TU Delft

Delft University of Technology

Document Version
Final published version

Licence
Dutch Copyright Act (Article 25fa)

Citation (APA)
Malschaert, D., Mohabeddine, A., Veljkovic, M., Leonetti, D., & Maljaars, J. (2026). Microstructures of the heat-affected zone around a cold crack in weldments. *Journal of Constructional Steel Research*, *244*, Article 110436. https://doi.org/10.1016/j.jcsr.2026.110436

Important note
To cite this publication, please use the final published version (if applicable).
Please check the document version above.

Copyright
In case the licence states “Dutch Copyright Act (Article 25fa)”, this publication was made available Green Open Access via the TU Delft Institutional Repository pursuant to Dutch Copyright Act (Article 25fa, the Taverne amendment). This provision does not affect copyright ownership.
Unless copyright is transferred by contract or statute, it remains with the copyright holder.

Sharing and reuse
Other than for strictly personal use, it is not permitted to download, forward or distribute the text or part of it, without the consent of the author(s) and/or copyright holder(s), unless the work is under an open content license such as Creative Commons.

Takedown policy
Please contact us and provide details if you believe this document breaches copyrights.
We will remove access to the work immediately and investigate your claim.

This work is downloaded from Delft University of Technology.

Journal of Constructional Steel Research 244 (2026) 110436

Contents lists available at ScienceDirect

Journal of Constructional Steel Research

journal homepage: www.elsevier.com/locate/jcsr

Microstructures of the heat-affected zone around a cold crack in weldments

David Malschaert [a,b,*], Anis Mohabeddine [a], Milan Veljkovic [a], Davide Leonetti [c], Johan Maljaars [c,d]

[a] Department of Engineering Structures, Delft University of Technology, Stevinweg 1, Delft, 2628 CN, The Netherlands
[b] Department of Steel and Movable Structures, Iv-Infra, Waarderweg 40, Haarlem, 2031 BP, The Netherlands
[c] Department of Built Environment, Eindhoven University of Technology, Groene Loper 3, Eindhoven, 5612 AZ, The Netherlands
[d] Department of Structural Reliability, TNO, Molengraaffsingel 8, Delft, 2629 JD, The Netherlands

ARTICLE INFO

Keywords:
T-joint
Tack welds
Heat-affected zone
Weld defect
Cold crack
Microstructure simulation

ABSTRACT

This paper presents a numerical and experimental study of three subregions within the heat-affected zone (HAZ) in the vicinity of a cold crack. The welding process of a T-joint assembly, including the tack welding process, was modelled in the finite element method utilising a transient heat-transfer analysis to capture the complete temperature history in the HAZ subregions. Temperature–time curves derived from the welding model, corresponding to the position of these subregions, were subsequently adopted as thermal loadings on physical coupon specimens using a Gleeble 3800 apparatus. The following subregions of the HAZ were experimentally simulated: intercritical HAZ, fine-grained HAZ, and coarse-grained HAZ. The results showed that the microstructures of the experimentally simulated HAZ subregions corresponded well with those found in the actual HAZ subregions near a cold crack in a sample taken from a bridge. Finally, the cooling rates from the tack welding process, in the absence of preheating, may lead to a microstructure that is sensitive to cold cracking in S355J2+N.

1. Introduction

Welded steel bridges and other welded steel structures from the 1950s up to 1970s were constructed according to the best welding practices of welded connections at that time, which have improved since then. Field inspections identified recurring weld defects in bridges erected during that period [1], like cold cracks. Cold cracks are overcome in current constructions by improvements in welding procedures and the weldability of structural steel grades. However, research on assessing the influence of cold cracks on the structural integrity of existing structures is of great importance [2]. Understanding how these cold cracks formed in old structures and developing accurate models to predict their growth when subjected to fatigue loading is of paramount importance to asset owners.

Welded plated girders require tack welds before the first continuous welding pass can be applied. As the microstructure of the steel highly depends on the cooling rate, the microstructure surrounding a tack weld can be different from that surrounding a normal weld. Tack welds are generally created using low-energy heat input welding, leading to high cooling rates and a more brittle microstructure that can be more prone to cold cracking than normal welds [3]. Pre-heating prior to welding was often required for the normalised structural steel grades erected during the indicated period. However, there are indications that pre-heating was not always applied for tack welding. Tack welds can either be incorporated or completely melted when welding over them. Subsequently, defects in the tack weld can either be retained or removed. The weld pass over the tack weld also affects its heat-affected zone (HAZ) by tempering and/or re-austenitising the microstructure, leading to a softer and tougher material [4]. Several reports have indicated fatigue cracks initiated at the location of tack welds [5,6]. Understanding how these cold cracks can form and understanding the microstructures around a cold crack is important to improve fatigue crack growth models for such weld defects.

Cold cracks, also known as hydrogen-induced cracking (HIC), typically occur in the heat-affected zone (HAZ) or the weld metal of a welded joint after the welding process is completed [7]. Cold cracks in steel structures generally form in regions of high hardness and high residual stress within the HAZ [8]. High hardness is related to the high cooling rate and the microstructure [9], and in particular to the carbon equivalent, while high residual stress [10] is associated with the welding process and constraints upon cooling. In addition, the presence of hydrogen has been demonstrated to play a significant role [11]. Whereas there is consensus on the conditions and prerequisites for cold-crack sensitive microstructures, whether or not cold

* Corresponding author at: Department of Engineering Structures, Delft University of Technology, Stevinweg 1, Delft, 2628 CN, The Netherlands.
E-mail address: D.H.Malschaert@tudelft.nl (D. Malschaert).

https://doi.org/10.1016/j.jcsr.2026.110436
Received 4 December 2025; Received in revised form 27 April 2026; Accepted 28 April 2026
Available online 6 May 2026
0143-974X/© 2026 Published by Elsevier Ltd.

Nomenclature

Latin symbols

A_{C1}	Temperature corresponding to onset of austenisation during heating
A_{C3}	Temperature corresponding to complete austenisation during heating
b	Half width of the double ellipsoid heat source
c_1	Front length of the double ellipsoid heat source
c_2	Rear length of the double ellipsoid heat source
C_{eq}	Carbon equivalent
d	Depth of the double ellipsoid heat source
H	Stiffener height
I	Electric current
L	Specimen length
Q	Power input
T_{max}	Maximum temperature
T_B	Base plate thickness
T_S	Stiffener thickness
U	Potential difference
v	Welding speed
W	Base plate width

Greek symbols

$\Delta t_{8/5}$	Cooling time from 800 °C to 500 °C
η	Welding efficiency

Acronyms

CGHAZ	Coarse-grained heat-affected zone
FEA	Finite element analysis
FGHAZ	Fine-grained heat-affected zone
HAZ	Heat-affected zone
HIC	Hydrogen-induced cracking
ICHAZ	Intercritical heat-affected zone
SSPT	Solid-state phase transformation

cracks actually develop is a matter of probability. In addition to the cold crack sensitivity of the chemical composition, expressed through the carbon equivalence, this probability depends on the spatial variability of chemical composition, pre-heating, welding process parameters, boundary conditions and hydrogen content of the electrode [12]. In addition, a specific thermal history and the chemical composition can lead to different microstructures for different steel grades. However, the transformation temperatures (AC1 and AC3) account for these aspects.

Fig. 1 presents a non in-scale example of the heat-affected zone within a butt welded connection. The heterogeneous microstructure of the HAZ can be subdivided into intercritical HAZ (ICHAZ), fine-grained HAZ (FGHAZ) and coarse-grained HAZ (CGHAZ) [13]. These regions differ from each other by the maximum temperature reached during the welding process [14]. The ICHAZ, is in between the starting point of austenisation (approximately at 725 °C) and the point at which austenisation is completed (approximately at 845 °C). Therefore, ICHAZ undergoes a partial phase transformation [15]. The maximum temperatures of both the FGHAZ and the CGHAZ are above the point of full phase transformation and the entire microstructure is austenised upon heating [16]. The maximum temperature of CGHAZ is significantly higher than that of FGHAZ, leading to coarser grains [17] and cold cracks typically appear in the CGHAZ, characterised by a relatively high hardness and brittle microstructure [13]. Due to cyclic loading, these cracks grow from the CGHAZ into the FGHAZ and ICHAZ regions before ultimately reaching the base metal. Although the HAZ is usually relatively thin compared to the overall thickness of the plate, the early growth of cold cracks located in the HAZ can represent a significant fraction of the overall fatigue life as the growth rate is still relatively low at this stage of the crack [18]. Therefore, quantifying the crack growth behaviour in the HAZ is important.

The influence of the microstructure on the fatigue crack growth rate has been a subject that holds opposing views in the literature. Some researchers regarded the effects of the microstructure as negligible, such as [20]. Others state significant differences [21]. Kim et al. [22] investigated the fatigue crack growth rates for the CGHAZ, FGHAZ and ICHAZ for high-strength steel HSB800 and established crack growth curves for these different microstructures. The ICHAZ and CGHAZ showed the highest crack growth rates, followed by the FGHAZ and then the base metal. The fatigue behaviour of the CGHAZ and FGHAZ regions for 18CrNiMo7-6 steel was studied in [23,24]. The CGHAZ was found to have a higher crack growth rate than the FGHAZ. To the knowledge of the authors, there has been no published experimental study into the influence of microstructures for normalised steels with a nominal yield stress of approximately 350 MPa, commonly used in structures such as bridges.

Field inspection reports on bridges identified the presence of several weld defects at various locations. These defects were pores, slag inclusion, lack of fusion and cold cracks. Fig. 2 shows a cold crack observed on an existing bridge constructed in the 1970s. Such defects were found in the weld between a stiffener and the flange of the main girder. Fig. 2(a) shows that the cold crack extended from the weld root of the tack weld up to the end of the fusion zone of weld Pass 1 over the tack weld. The crack was located in the CGHAZ as shown in Fig. 2(b), which is usually the location for cold cracks due to the increased hardness of the CGHAZ [25]. Fig. 2(c) shows the microstructure at the crack tip. The tip of the crack ends at the fusion line of Pass 1 over the tack weld. This indicates that this crack initiated after the tack weld was applied. Upon applying Pass 1 over the tack weld, the crack did not extend. Fig. 2(a) presents the main loading direction with respect to the defect. When the crack would propagate from its initial orientation, the expected growth path is through the HAZ into the base metal.

Studying the HAZ of welded connection can be an arduous task due to the inherent inhomogeneous microstructure and the narrowness of each individual microstructural zone [22]. In order to quantify the mechanical properties of a subregion, experimental simulation utilising a Gleeble apparatus is often employed, but this is accompanied by other difficulties. Firstly, the high cooling rates that occur in welding are hard to reach in such tests and a homogeneous cooling rate on a larger region is even more difficult to achieve [23].

Between the introduction of weldments in bridges (around 1950) and 1980, several comparable cold cracks have been found in multiple bridges constructed around 1970. When exposed to fluctuating loads, a fatigue crack may grow from the cold crack, through the HAZ into the base metal. Therefore, it is important to understand the mechanical behaviour of the microstructural layers of the HAZ. To quantify this, destructive tests are needed for which the different HAZ subregions in an actual weldment are too small. In the current study, a method was developed for reproducing microstructures of the HAZ subregions on separate specimens that are large enough for further (destructive) testing (such as fracture tests, crack growth tests and tensile tests).

The HAZ subregions in the expected growth path of a cold crack are reproduced on larger coupon-shaped specimens. A numerical analysis is performed to model the execution process of a tack weld that may lead to a cold crack, followed by the subsequent full weld pass 1 over the tack weld. The microstructures of the HAZ subregions were experimentally simulated using a Gleeble 3800 apparatus utilising the temperature–time curves from the numerical analysis. These microstructures are compared with the microstructures found in a sample taken from a bridge containing a cold crack.

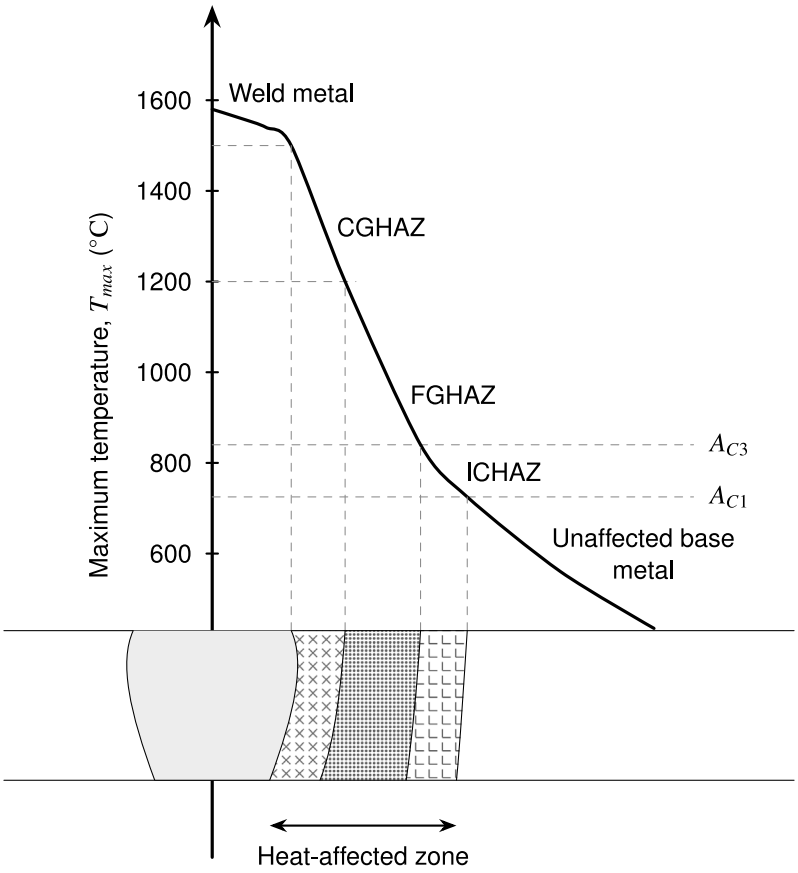


Fig. 1. Schematic representation of HAZ subregions in a butt welded connection (based on [19]).

2. Materials and methods

2.1. Material

Three different hypoeutectoid steels were considered, referred to as Steel A, Steel B and Steel C. Table 1 presents the chemical compositions of the aforementioned steels, determined through optical emission spectroscopy, of which the carbon equivalent C_{eq} has been determined from [26]. The elements Mo, V, Nb and Ti had a wt% below 0.01 and the element B had a wt% below 0.001. For all steels considered, the elements C and Mn contributed most to the carbon equivalent value and hardness.

Steel A, with a nominal yield strength of 350 MPa, was taken from a bridge (as presented in Fig. 2) from the 1970s in which cold cracks were found in the flange of a main girder. Steel A had an average ferrite grain size of 14 μm and an average pearlite colony size of 9 μm. A hardness of 174 HV1 was measured for the base metal.

Steel B was recently produced and was of grade S355J2+N. As there was no material available for Steel A to conduct experiments with, a steel with a similar carbon equivalent C_{eq} to Steel A was used. The resulting microstructure from the experiments on Steel B are subsequently compared to those from Steel A. Fig. 3 presents the microstructure of the base metal. It had an average ferrite grain size of 13 μm and an average pearlite colony size of 11 μm. A hardness of 162 HV1 was measured for the base metal.

Steel C, with a nominal yield strength of 235 MPa, was taken from the web of a main girder of an old disassembled bridge (other than the bridge from Fig. 2) which was constructed in 1970s. Fig. 3 presents the microstructure of the base metal. It had an average ferrite grain size of 23 μm and an average pearlite colony size of 13 μm. A hardness of 139 HV1 was measured for the base metal. While steels with a nominal yield strength and carbon equivalent values of Steel C a not considered sensitive to cold cracking, experiments where conducted in this study on Steel C for comparison.

Table 1
Chemical composition and carbon equivalent of the investigated steels given in wt%.

	C	Si	Mn	P	S	Cr	Cu	Ni	Al_{tot}	N	C_{eq}
Steel A	0.17	0.40	1.32	0.010	0.020	0.03	0.03	0.02	0.05	0.006	0.405
Steel B	0.15	0.19	1.40	0.015	0.009	0.05	0.03	0.02	0.03	0.003	0.397
Steel C	0.13	0.18	0.49	0.009	0.020	0.01	0.06	0.05	0.02	0.007	0.225

2.2. Sequence of study

Fig. 4 presents the sequence of study. A finite element model was developed to simulate the welding process through a heat-transfer analysis. This model simulated the tack welding, Pass 1 over the tack weld and Pass 2 on the opposite side of the stiffener and in opposite direction of Pass 1. The temperature–time curves were obtained from the finite element model around the location of this cold crack. These temperature–time curves were applied to coupon-shaped specimens of the base metals of Steel B and Steel C. The resulting microstructures of the HAZ substructures were finally analysed and a comparison was made to the microstructures around the cold crack found in the bridge from Fig. 2, constructed from Steel A.

3. Finite element modelling of the welding process

3.1. Methods

Fig. 5 and Table 2 present the geometry of the T-joint, derived from the sample of Fig. 2, and the direction of welding. The welding model

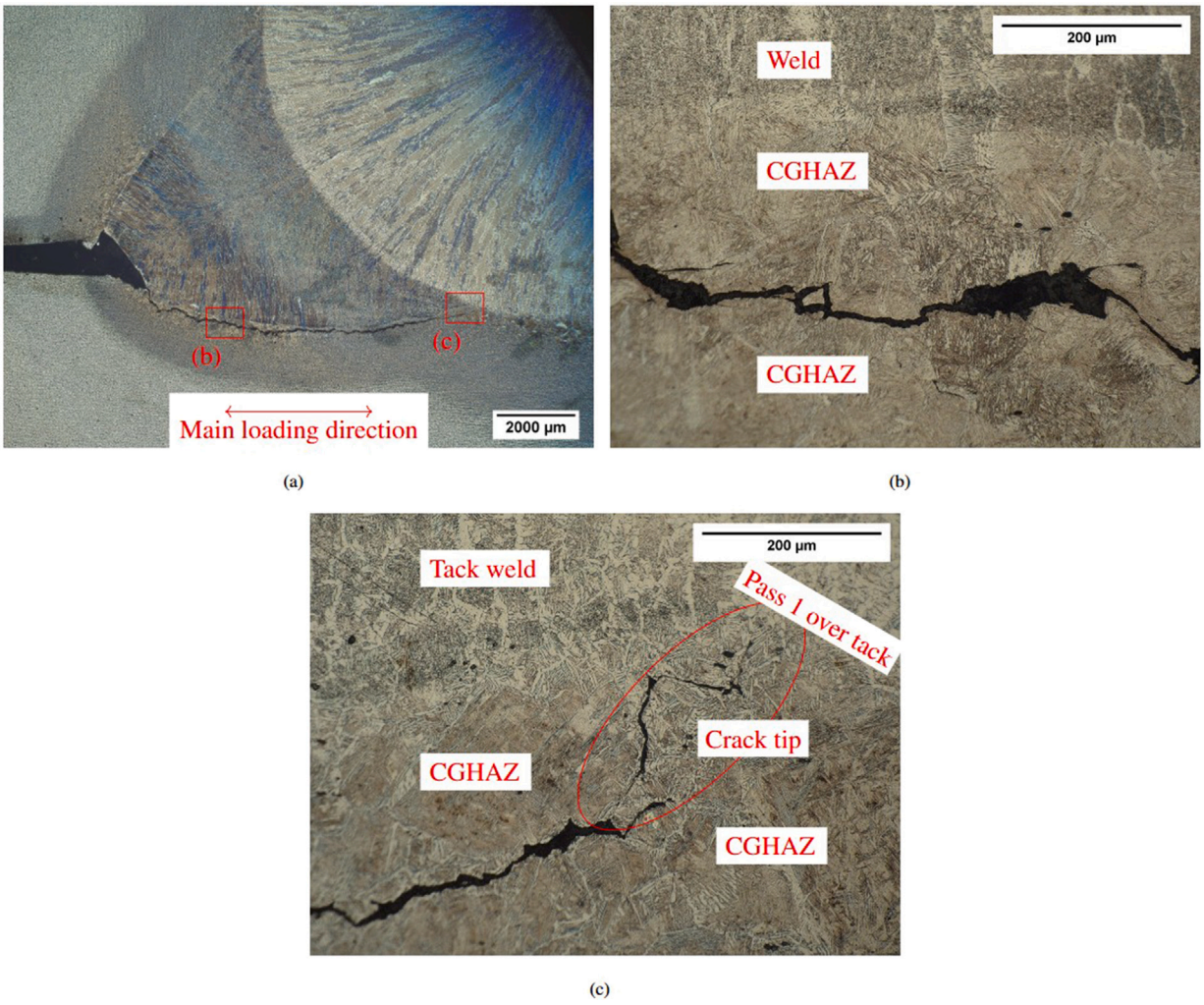


Fig. 2. Microscopic images of a sample of a weld taken from a bridge in the Netherlands containing a cold crack defect. This figure shows the overview of the weld with cold crack with magnification X20 (a), microstructure around the crack with magnification X500 (b) and the crack tip with magnification of X500 (c). The bridge was constructed in the 1970s and was made out of steel with a nominal yield stress of approximately 350 MPa. The defect was located in the weld of the main girder flange that had a thickness of 40 mm.

comprised the following steps: tack weld, Pass 1 over the tack weld and Pass 2, located on the opposite side of the stiffener and in opposite direction of Pass 1. The centre of the tack weld was located at a distance of 15 mm from the edge T-joint and with a length of 10.0 mm. The leg lengths the weld were 6 mm (see Fig. 5(b) for definition used). The FE-model uses an idealised weld geometry for the tack weld and the geometry of Pass 1 and Pass 2. This simplification might affect the exact position of the fusion boundary, the widths of HAZ layers and they might marginally affect the cooling rates. However, the overall thermal response is governed by the heat input, plate thicknesses and pre-heating conditions. The simplifications made in the FEA are insignificant for the resulting thermal cycles in the subregions of the HAZ. The presence of a pre-existing crack was not explicitly modelled as its influence remains local and does not affect the representative thermal cycles used in the current study.

A heat transfer analysis in Abaqus/CAE 2022 [27] was performed to model the welding of a fillet-welded T-joint. The modelling strategy is similar to that of a previous study conducted by the authors [28]. Main aspects and deviations with respect to [28] are mentioned hereafter. The heat transfer analysis included the tack welding process, cooling until ambient temperature, pre-heating of the entire T-joint to 200 °C (derived from [29]), Pass 1 over the tack weld, inter-pass cooling time of 5 s, Pass 2 on opposite side of the stiffener and final cooling up to ambient temperature. No pre-heating was included prior to applying the tack weld. The sub-modelling technique was utilised to refine the mesh around the tack weld in two steps. Fig. 6 show the global model and the submodels.

Table 2
T-joint geometry parameters (see Fig. 5 for the symbols).

L mm	W mm	H mm	T_B mm	T_S mm
200	200	100	40	10

Table 3
Welding- and Goldak heat source parameters.

b mm	d mm	c_1 mm	c_2 mm	U V	I A	η –	v mm s^{-1}
3	3	3	6	30	300	0.8	6

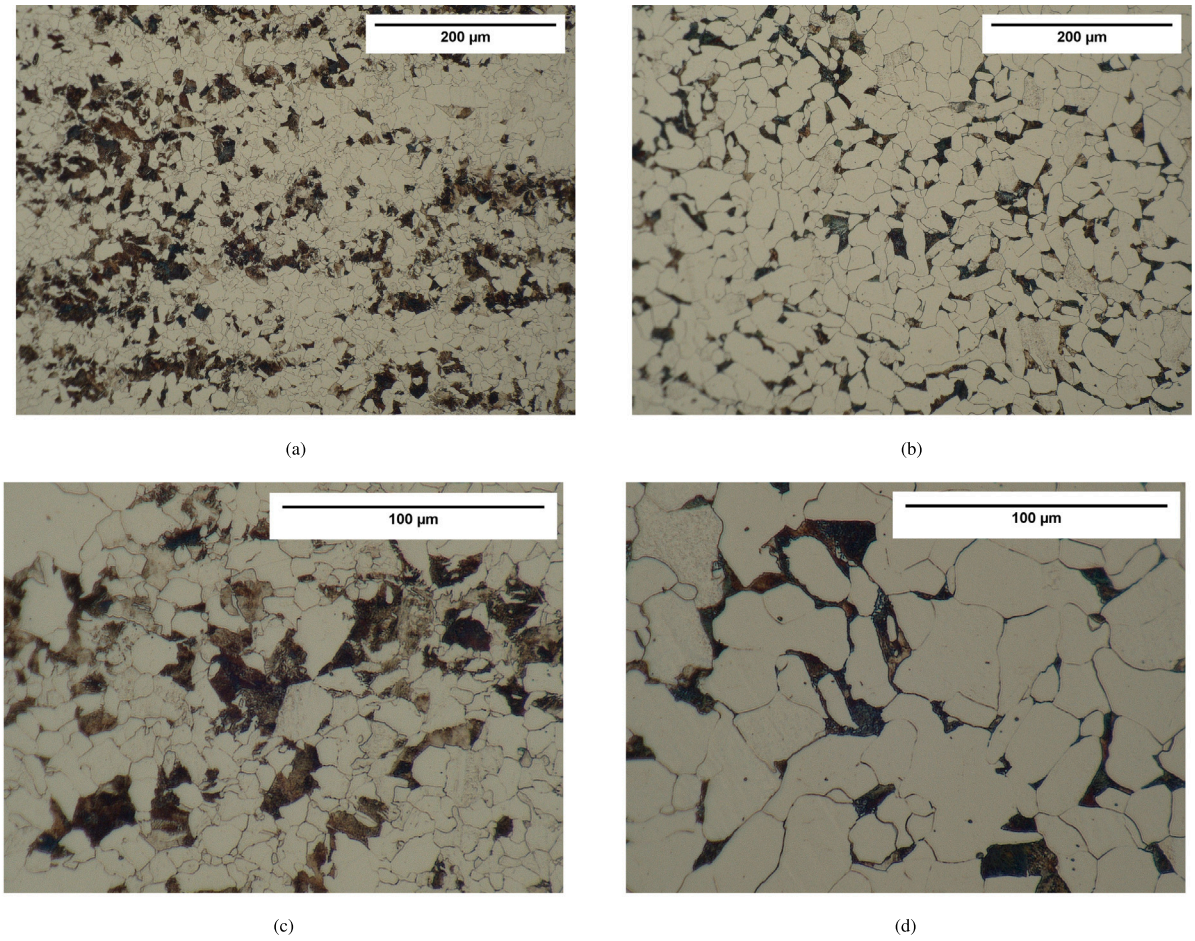


Fig. 3. Microstructures of the base metal of Steel B with magnifications of X500 (a) and 1500 (c) and Steel C with magnifications of X500 (b) and X1500 (d) utilised in the current experimental study.

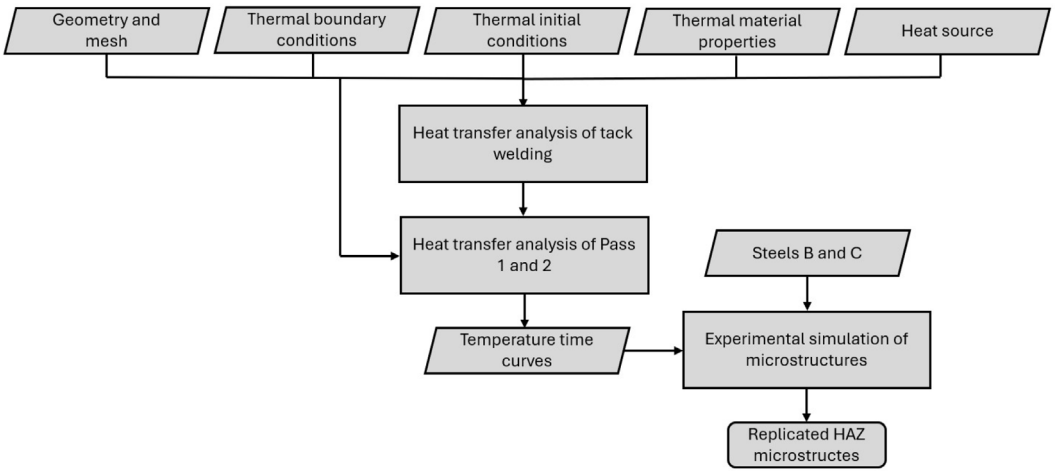


Fig. 4. Flow-chart of the sequence of study.

Quadratic brick elements with full integration were used of type DC3D20 for the heat transfer analysis. Average element sizes of 2.0 mm, 1.0 mm and 0.25 mm were used for the global model, first layer of sub-model and second layer of submodel, respectively. A mesh sensitivity study was conducted in previous work [28] and was used to design the mesh in the current model. Fig. 6 presents the meshing for the global model and submodels.

Table 3 presents the parameters for the Goldak heat source model [30] and the welding parameters. A heat input of 1.2 kJ mm^{-1} was used for the welding process. The heat input Q is the product of the potential difference U, the electric current I and the efficiency η divided by the travel speed v.

$$Q = \frac{U \cdot I \cdot \eta}{v} \tag{1}$$

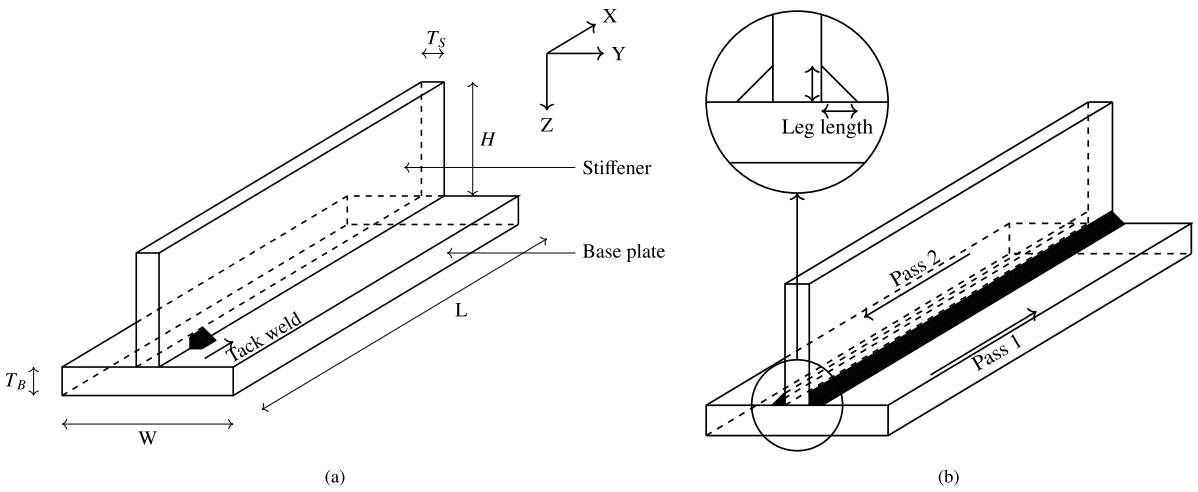


Fig. 5. Geometry of T-joint including tack weld (a) and Pass 1 and Pass 2 (b).

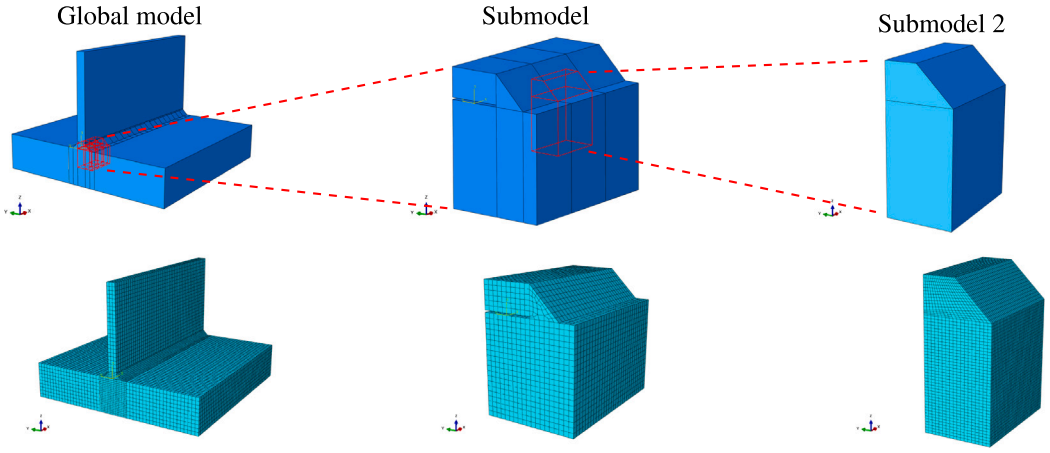


Fig. 6. Finite element model including the global model and first and second submodel. Top figures show the assembled structures including partitioning and the bottom figures show the meshed structures.

3.2. FEA results and discussion

Fig. 7 shows the temperature–time curves at discrete locations along the thickness direction of the base plate, halfway the tack weld length, throughout the welding process. In transverse direction, these temperature–time curves were at 2 mm away from the weld root, corresponding to the deepest point of the fusion line of the tack weld. The base plate is twice as thick as the stiffener and thus exhibits higher cooling rates due to the more material to conduct heat to. Therefore, the location most prone to cold cracking would be the HAZ at the location of the base plate (as was the case in the bridge sample, Fig. 2). The temperature corresponding to onset of austenisation during heating, A_{c1}, and the temperature corresponding to complete austenisation during heating, A_{c3}, are indicated in the graph and have been determined by the chemical composition of the material (see Table 1), These are determined by the following equations, following Eqs. (2) and (3) [31]:

$$A_{C1} = 742 - 29 \cdot C - 14 \cdot Mn + 13 \cdot Si + 16 \cdot Cr - 17 \cdot Ni - 16 \cdot Mo + 45 \cdot V + 36 \cdot Cu \quad (2)$$

$$A_{C3} = 925 - 219 \cdot \sqrt{C} - 7 \cdot Mn + 39 \cdot Si - 16 \cdot Ni + 13 \cdot Mo + 97 \cdot V \quad (3)$$

With A_{C1} and A_{C3} in °C and wt% for the constitutes. Table 4 presents the A_{C1} and A_{C3} values for all steels analysed.

Table 4
A_{C1} and A_{C3} values for each steel analysed in the current study determined through their chemical composition, values in °C.

	A_{C1}	A_{C3}
Steel A	725	840
Steel B	722	838
Steel C	735	849

The temperatures during and after applying the tack weld, Pass 1, and Pass 2 are indicated in the graph in Fig. 7. Application of the tack weld and Pass 1 led to temperatures above A_{c1} and A_{c3} whereas the peak temperature stayed below A_{c1} during Pass 2. As a result, no phase change is expected upon the application of Pass 2 and the influence of Pass 2 on the microstructure at the expected growth path of the cold crack was further neglected.

The distinction between the different HAZ subregions is based on the maximum temperature as follows [32]:

$$T_{max} = \begin{cases} [A_{C1}, A_{C3}] & \text{ICHAZ} \\ [A_{C3}, 1200\,°C] & \text{FGHAZ} \\ [1200\,°C, 1500\,°C] & \text{CGHAZ} \end{cases} \quad (4)$$

Table 5 presents the cooling time from 800 °C to 500 °C, $\Delta t_{8/5}$, for the FGHAZ and CGHAZ for both the tack weld and Pass 1. During the FEA of the tack welding process, a time of $\Delta t_{8/5} = 2.0$ s was found at

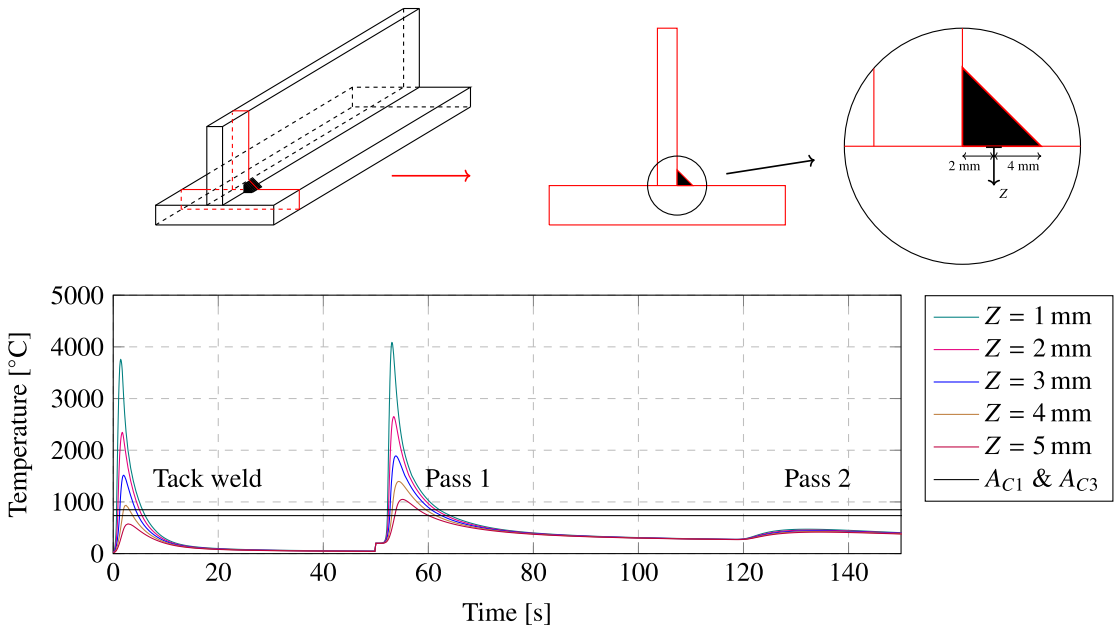


Fig. 7. Temperature–time curves recorded at the location of the tack weld from welding simulation of tack welding and subsequent Pass 1 and 2.

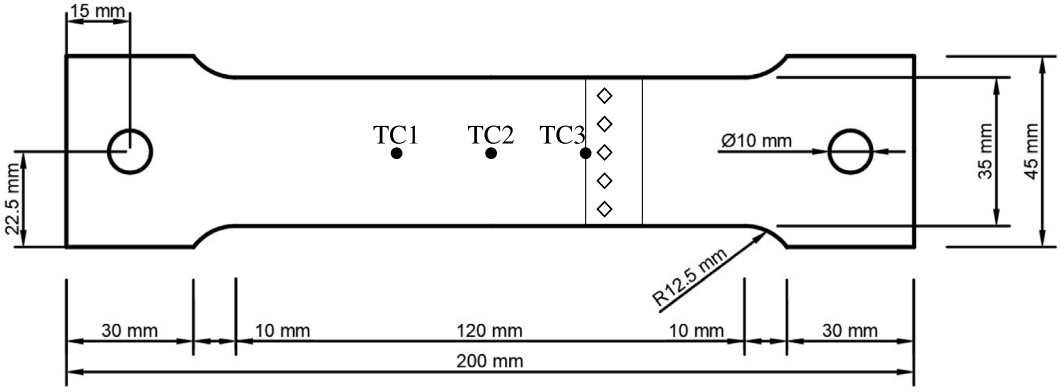


Fig. 8. Specimen used in Gleeble experiment, created from base metal of Steels B and C. The specimens had a thickness of 2 mm. The locations of the hardness measurements and thermocouples (TC) are indicated with ◇ and •, respectively. The rectangle represents the sample taken from the Gleeble specimen for metallographic analyses.

Table 5
$\Delta t_{8/5}$ in s resulting from the welding simulation at the CGHAZ and FGHAZ of tack welding and Pass 1.

	Tack welding	Pass 1 over tack weld
FGHAZ	2.0	9.4
CGHAZ	2.0	9.1

the CGHAZ. This cooling rate is close to that of [25] ($\Delta t_{8/5}$ = 1.5 s), which led to cold cracks in each specimen for S355 steel with a similar chemical composition for underwater wet welding. As the cooling rate is the driving force that determines the microstructure [32], the current thermal cycle of the tack welding process leads to a microstructure sensitive to cold cracking. Consequently, preheating prior to tack welding reduces cooling rates and thereby prevents the formation of microstructures susceptible to cold cracking.

4. Experimental simulation of microstructure

4.1. Methods

The microstructures of the HAZ subregions, namely ICHAZ, FGHAZ and CGHAZ, were simulated on coupon-shaped specimens using a Gleeble 3800 apparatus, a thermal-mechanical simulator that provides precise control of temperature.

Three Gleeble simulations were performed for each region on specimens with dimensions presented in Fig. 8. Table 6 presents an overview of the temperature–time curves used in the Gleeble simulations. The temperature–time curves correspond to Pass 1, recorded at the location of the tack weld, resulting from the simulation described in Section 3.1. These temperature–time curves were defined for each HAZ subregion individually and were composed of a heating rate, dwell time at the maximum temperature T_{max}, and cooling rates. Fig. 9 presents the test set-up. The tests were executed in vacuum to avoid oxidation during the experimental simulation. Two nozzels were used from which the cooling medium was exerted. Cooling was applied with a combination of nitrogen gas and water. After the specimens were cooled to a temperature of 300 °C, they were further cooled down to room temperature

Table 6
Thermal cycle input for microstructure simulations using Gleeble.

Region	Heating rate $[20 - T_{max}]$ °C °C s^{-1}	Dwell time $[T_{max}]$ °C s	Cooling rate $[T_{max} - 800]$ °C °C s^{-1}	Cooling rate $[T_{max} - 500]$ °C °C s^{-1}	Cooling rate [500–300] °C °C s^{-1}
ICHAZ	130	2	–	25	7
				[800–500] °C	
FGHAZ	200	2	70	30	7
CGHAZ	300	2	90	30	7

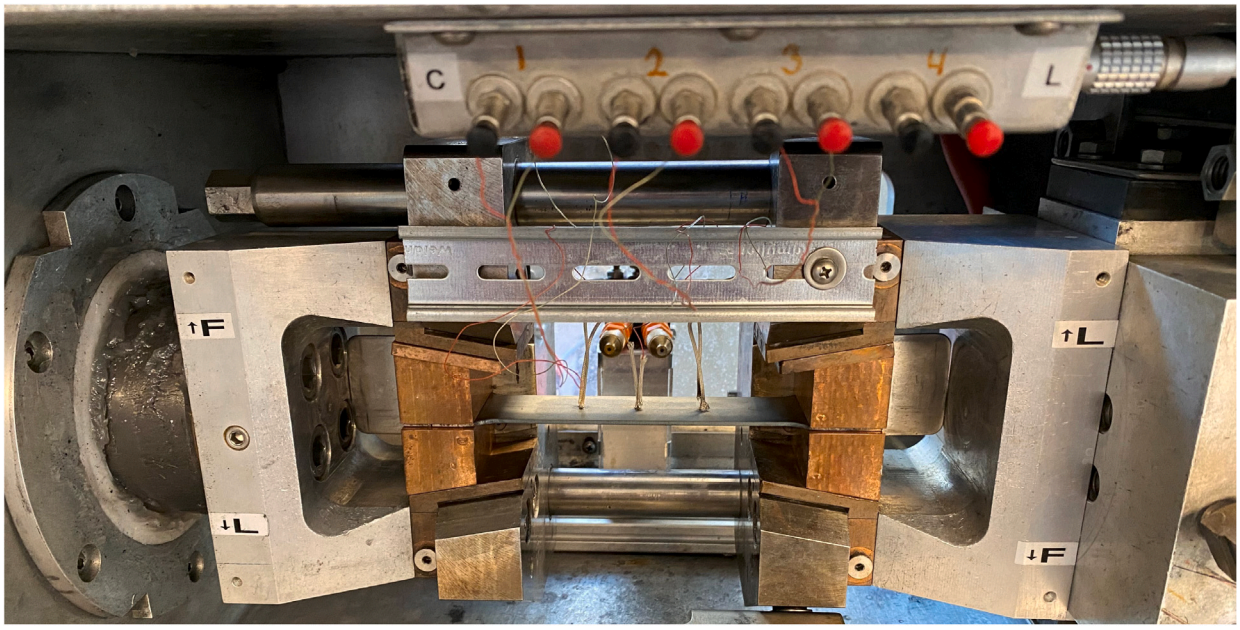


Fig. 9. Experimental set-up of the Gleeble.

using only nitrogen gas. Three thermocouples were spot welded to the specimen to monitor the temperature during the experiment out of which the middle thermocouple was used as feedback to the Gleeble apparatus (TC2 in Fig. 8). A tensile load of 0.8 kN (corresponding to 11 MPa) was maintained throughout the experimental simulation to maintain contact between the copper grips and the specimen. Due to the low stiffness at maximum temperature for the CGHAZ simulation, the tensile load for the CGHAZ was reduced to 0.4 kN (corresponding to 5 MPa).

After the Gleeble simulations, samples were taken from the specimens (indicated by the rectangle in Fig. 8) as well as from the base metal for metallographic analysis. The samples were polished and then etched with 2 % Nital. Vickers hardness tests (HV1) were performed at five locations indicated in Fig. 8, and the average was taken. The hardness was compared to that from the heat affected zone of the actual welded joint of Steel A.

4.2. Experimental results and discussion

Figs. 10 to 12 present the microstructures of the simulated HAZ sub-regions for Steel B and Steel C. These are displayed with a X500 and a X1500 magnification. The figure also shows a comparison of the temperature–time curves from the finite element analysis of the welding process and the thermocouple measurements (see Fig. 8 for position of thermocouples).

Fig. 10 presents the microstructure of the experimentally simulated ICHAZ. The T_{max} = 792 °C value of the simulated ICHAZ is between A_{c1} and A_{c3} (see Table 4) resulting in partial austenisation SSPT. The microstructures of Steel B and C show large ferrite grains that remained untransformed after the thermal cycle corresponding to the ICHAZ. Along the boundaries of the untransformed ferrite there are more refined regions that resulted from the partial austenite transformation upon heating. The dark gray regions are pearlite colonies that are significantly refined as compared to the pearlite of the base metal (see Fig. 3). In addition, refined ferrite grains were found adjacent to the refined pearlite colonies. Upon heating, pearlite colonies transform at lower temperatures than ferrite grains [33]. When T_{max} is above this level but below the level of the transformation temperature of the ferrite grains, the pearlite colonies undergo SSPT whereas the ferrite grains do not. Then, upon cooling, the prior pearlite colonies are transformed from the austenite phase to refined ferrite/pearlite. This is also the reason why the refined ferrite/pearlite is grouped around the larger untransformed ferrite grains. The transformation of the pearlite colonies into refined ferrite/pearlite was also obtained by Eroğlu and Aksoy [34]. An average size of 13 μm and 20 μm was measured for the untransformed ferrite grains in the ICHAZ of Steel B and C, respectively. This is similar to the average ferrite grain size of their respective base metal (see Section 2.1). An average size of 2 μm and 4 μm was measured for the refined ferrite grains and refined pearlite colonies of the simulated ICHAZ of Steel B and C, respectively.

Fig. 11 presents the microstructure of the experimentally simulated FGHAZ. The T_{max} = 1025 °C was above A_{c3} (see Table 4) which implies that the entire microstructure of the specimen was transformed to austenite phase. Upon cooling, the austenite phase transformed to a combination of ferrite, pearlite and bainite in Steel B and a ferrite/pearlite phase for Steel C. The grains/colonies were much more refined as compares to their respective base metal (see Section 2.1). In Steel B, an average size of 4 μm and 2 μm was measured for the ferrite grains and pearlite colonies, respectively. These values were 10 μm and 5 μm for Steel C.

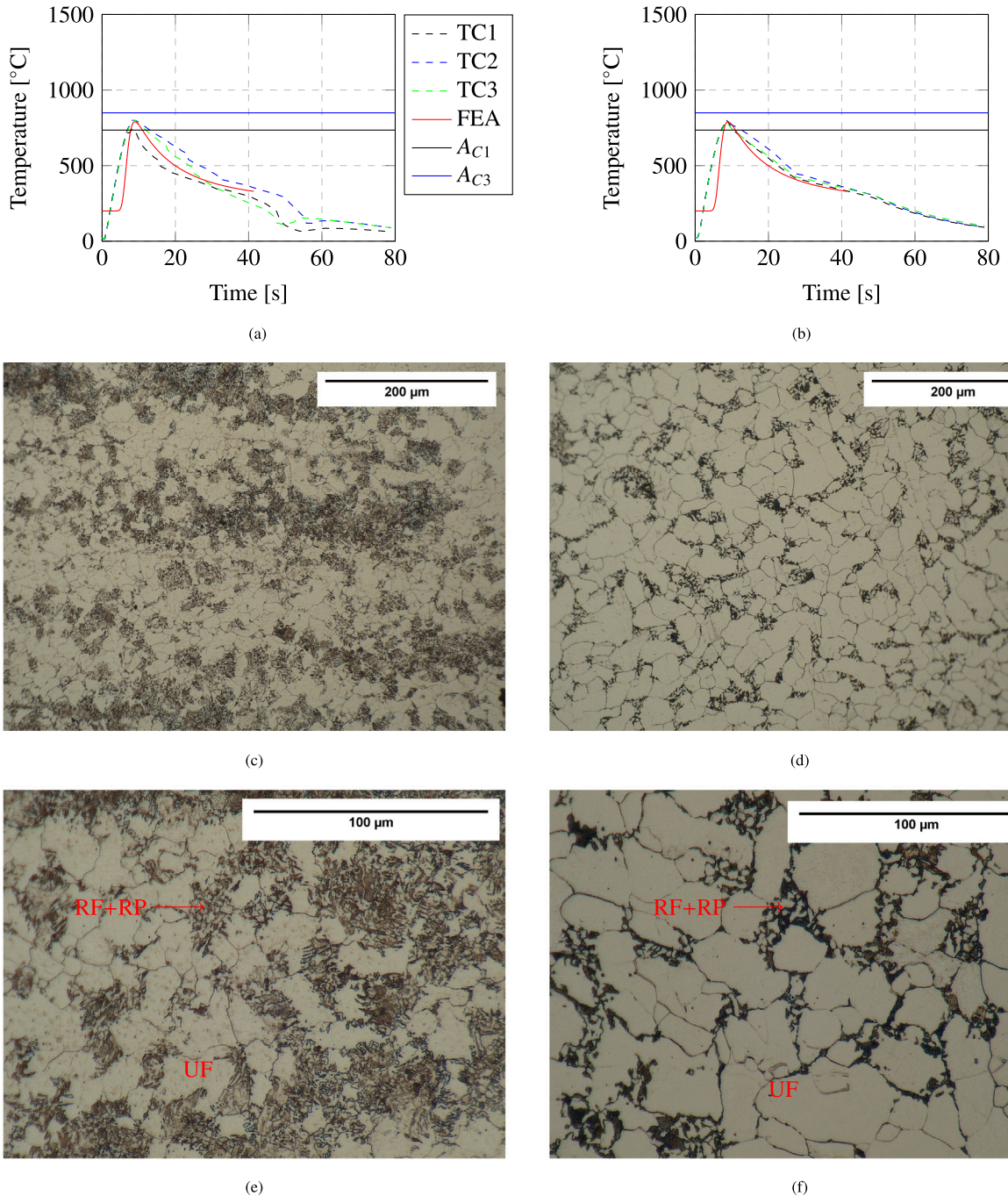


Fig. 10. Temperature–time curves of the simulated ICHAZ subregion from FEA and thermocouple (TC) measurements of Steel B (a) and Steel C (b). Microscopic images of simulated ICHAZ of Steel B with magnifications of X500 (c) and X1500 (e) and simulated ICHAZ of Steel C with magnifications of X500 (d) and X1500 (f), UF=untransformed ferrite, RF= refined ferrite and RP=refined pearlite.

Fig. 12 shows the microstructure of the experimentally simulated CGHAZ. Its microstructure is clearly distinct from the other simulated HAZ subregions and the base metal. Similar to the simulated FGHAZ, the T_{max} = 1350 °C of the simulated CGHAZ was above A_{c3} (see Table 4). Subsequently, as the cooling rate was higher than that of the FG-HAZ (see Table 6), a bainite/martensite microstructure formed which is characterised as harder and more brittle than the ferrite/pearlite microstructures of the other HAZ subregions [35].

5. Comparison to bridge sample

Although the exact welding conditions of the samples extracted from the bridge (as presented in Fig. 2) are unknown, a comparative analysis is conducted between the microstructures observed near the cold crack in the sample of the bridge (Steel A) and those obtained in this experimental study for Steel B and Steel C. This comparison aims to evaluate the accuracy of the simulated microstructures in replicating the HAZ present in the bridge sample. Fig. 13 presents a side-by-side visualisation of the microstructures corresponding to the base material, ICHAZ, FGHAZ and CGHAZ in the real HAZ of Steel A and the experimentally simulated HAZ of Steel B and Steel C.

After closer examination of the ICHAZ of Steel A, B and C, large ferrite grains comparable with those found in the base material of that steel were identified in all samples (ca. 13 µm for Steel A and B and ca. 22 µm for Steel C). Among these large untransformed ferrite grains,

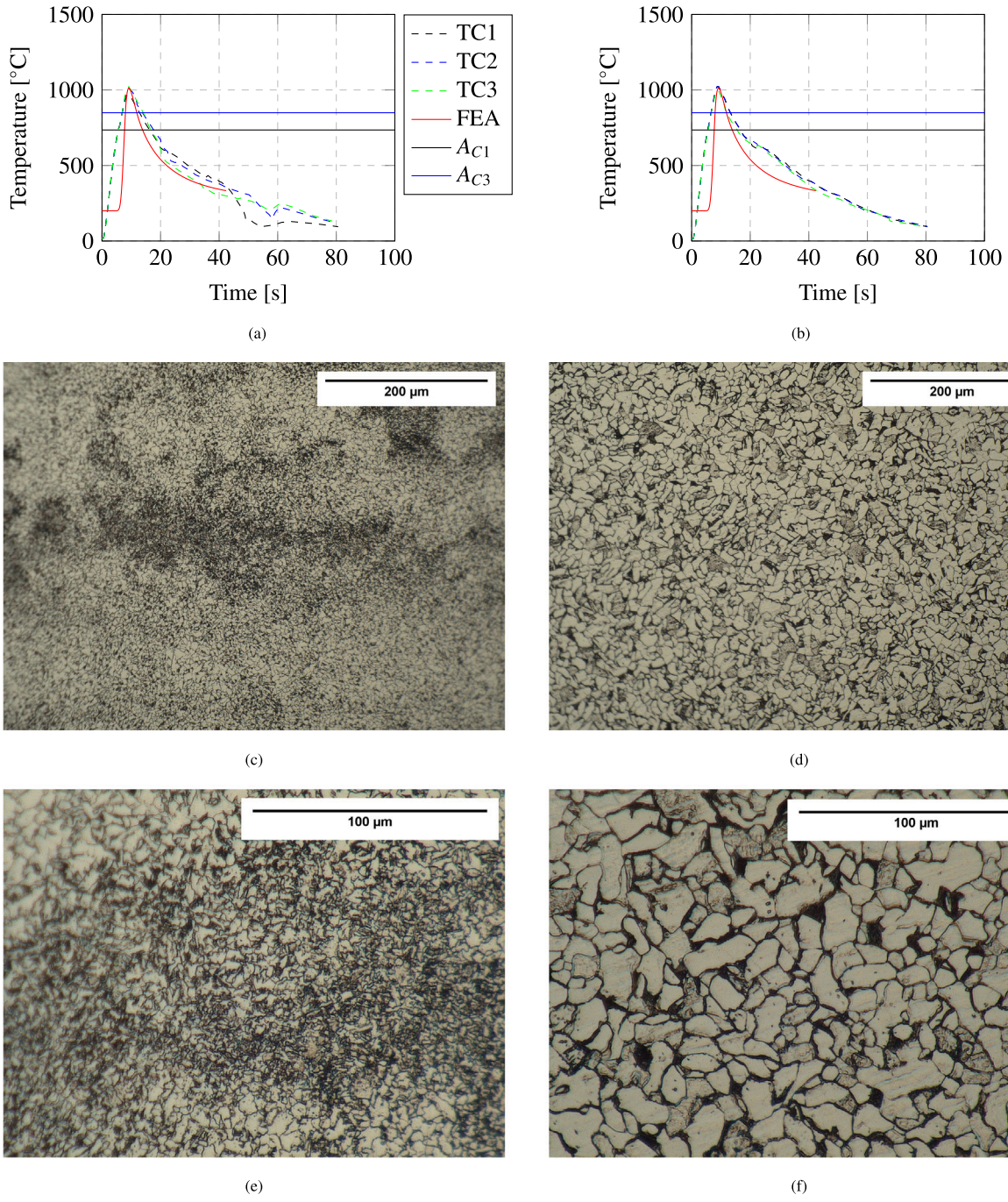


Fig. 11. Temperature–time curves of the simulated FGHAZ subregion from FEA and thermocouple (TC) measurements of Steel B (a) and Steel C (b). Microscopic images of simulated FGHAZ of Steel B with magnifications of X500 (c) and X1500 (e) and simulated FGHAZ of Steel C with magnifications of X500 (d) and X1500 (f).

groups of refined ferrite grains and refined pearlite colonies were found at the positions of the former pearlite colonies. This phenomenon is attributed to the partial austenisation that occurs in the ICHAZ, where pearlite dissolution occurs, followed by rapid cooling, which promotes the formation of a fine-grained microstructure. The refined ferrite and pearlite had a size of approximately 2 µm for Steel A and B and approximately 4 µm for Steel C, respectively.

Significant grain refinement was observed in the FGHAZ of both the bridge sample and the experimentally simulated samples as a result of limited austenite grain growth upon heating. The grains in Steel A and B were smaller (approximately. 2 µm) than those of Steel C (approximately. 7 µm), which is a consequence from the initially smaller grain sizes of their corresponding base material.

The real CGHAZ of Steel A and the simulated CGHAZ of Steels B and C showed a bainitic/martensitic microstructure, associated to the high cooling rate of this region.

Fig. 14 shows the locations where Vickers hardness (HV1) tests were performed on the sample from the bridge containing a cold crack. Measurements were taken in the weld metal, CGHAZ, FGHAZ, ICHAZ and base metal along the expected crack growth path from the initial cold crack at the tack weld. Additional measurements were taken just above the cold crack in the CGHAZ. Finally, hardness measurements were also taken from the weld metal, CGHAZ, FGHAZ and ICHAZ of

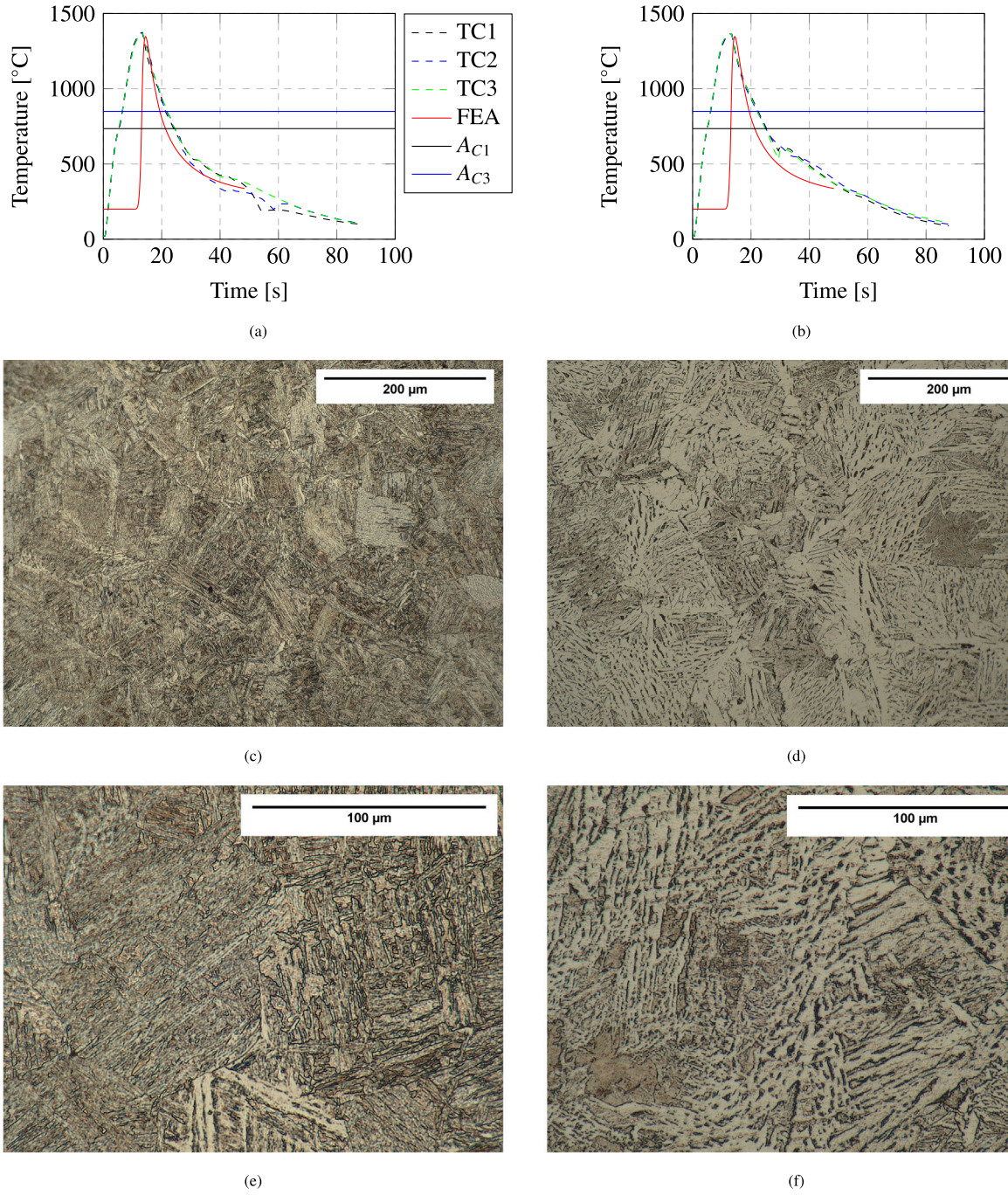


Fig. 12. Temperature–time curves of the simulated CGHAZ subregion from FEA and thermocouple (TC) measurements of Steel B (a) and Steel C (b). Microscopic images of simulated CGHAZ of Steel B with magnifications of X500 (c) and X1500 (e) and simulated CGHAZ of Steel C with magnifications of X500 (d) and X1500 (f).

Pass 1 over the tack weld. Fig. 15 presents the aforementioned hardness results alongside those of the experimentally simulated HAZ of Steel B and C and their base metal.

The hardness of the base metal of Steel B and C were approximately 7 % and 20 % lower, respectively, than that of Steel A. In all steels studied, the hardness increased when studying a HAZ subregion closer to the fusion line. For Steel A, the weld metal had a hardness of approximately 214–218 HV1, which was lower than the CGHAZ. The hardness results of Steel B corresponded well with the hardness along the expected growth path of the cold crack in Steel A with a difference of approximately 20 %, 10 % and 19 % for the ICHAZ, FGHAZ and CGHAZ, respectively.

Although the cold crack formed in the tack weld region of Steel A, the CGHAZ of Pass 1 over the tack weld was significantly harder than the CGHAZ of the tack weld itself. This is attributed to tempering of the material near the tack weld during the process of applying Pass 1 over the tack weld. At the time of cold crack nucleation, the local hardness

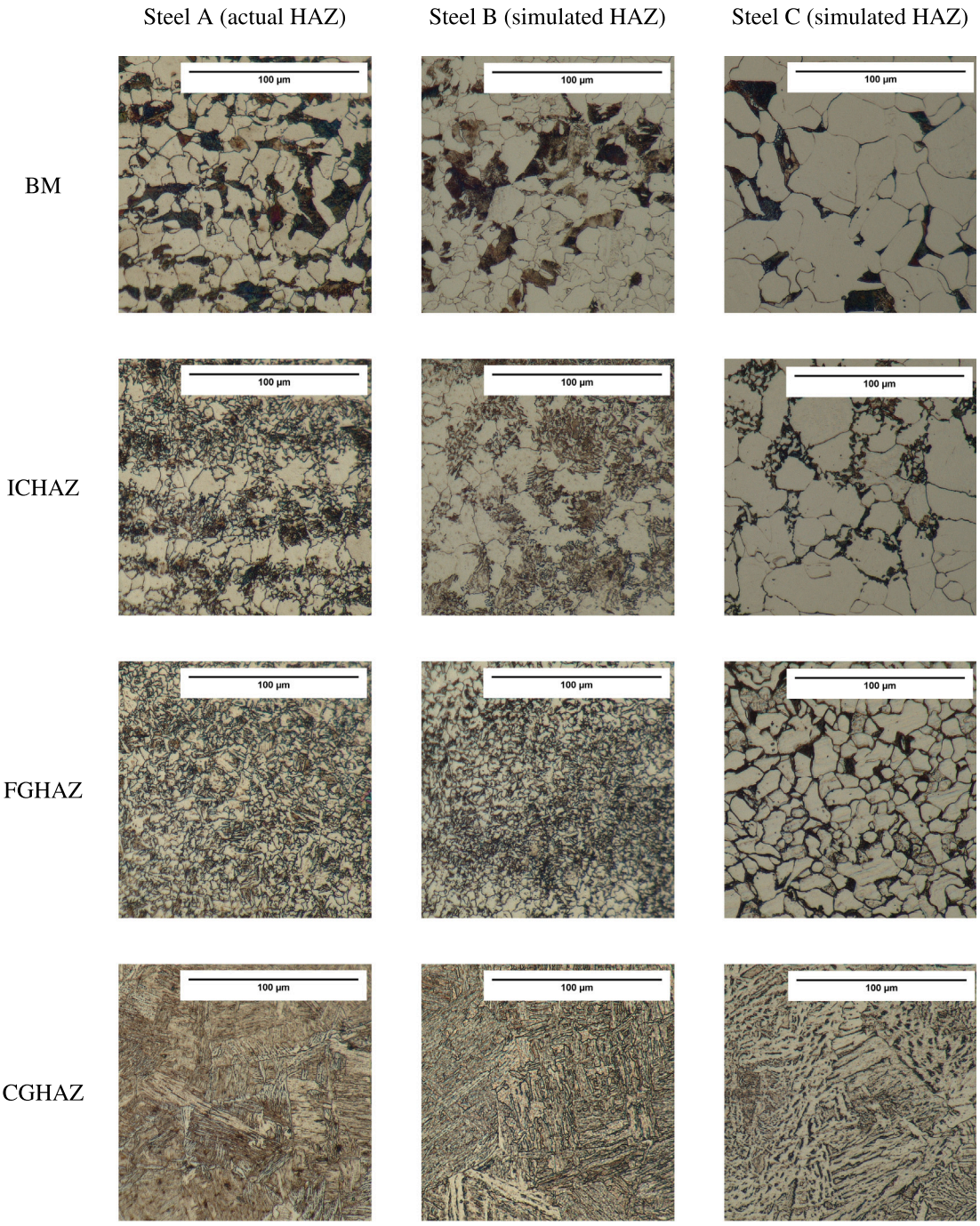


Fig. 13. Comparison of microstructures of BM and different HAZ subregions of a real welded connection of steel A and the BM and simulated HAZ of Steel B and Steel C. Magnification of X1500 was used.

may have been much higher and was subsequently decreased after Pass 1 over the tack weld was applied.

The authors conclude that the microstructures of the HAZ found in the expected growth path of the cold crack in Steel A have been accurately experimentally simulated using Steel B. The type of microstructures of each experimentally simulated subregion of Steel B and Steel C corresponded well with those found in Steel A. Furthermore, the microstructural morphologies of the ICHAZ and FGHAZ were of equal size between Steel A and B. The hardness of the experimentally simulated subregions of Steel B were within 20 % of those found in Steel A. The CGHAZ of Steel B was slighly harder than that of Steel A and as such steel B should be considered prone to cold cracking when exposed to cooling rates from tack welding process in the absence of preheating. All hardness results of Steel C were significantly lower than those of Steels A and B and is less likely to be prone to cold cracking.

6. Concluding remarks

A finite element transient heat-transfer analysis was performed of the tack welding and the subsequent two weld passes. Preheating prior to tack welding was not performed – a typical weld procedure applied in structures constructed in the years 1950–1970 – to determine

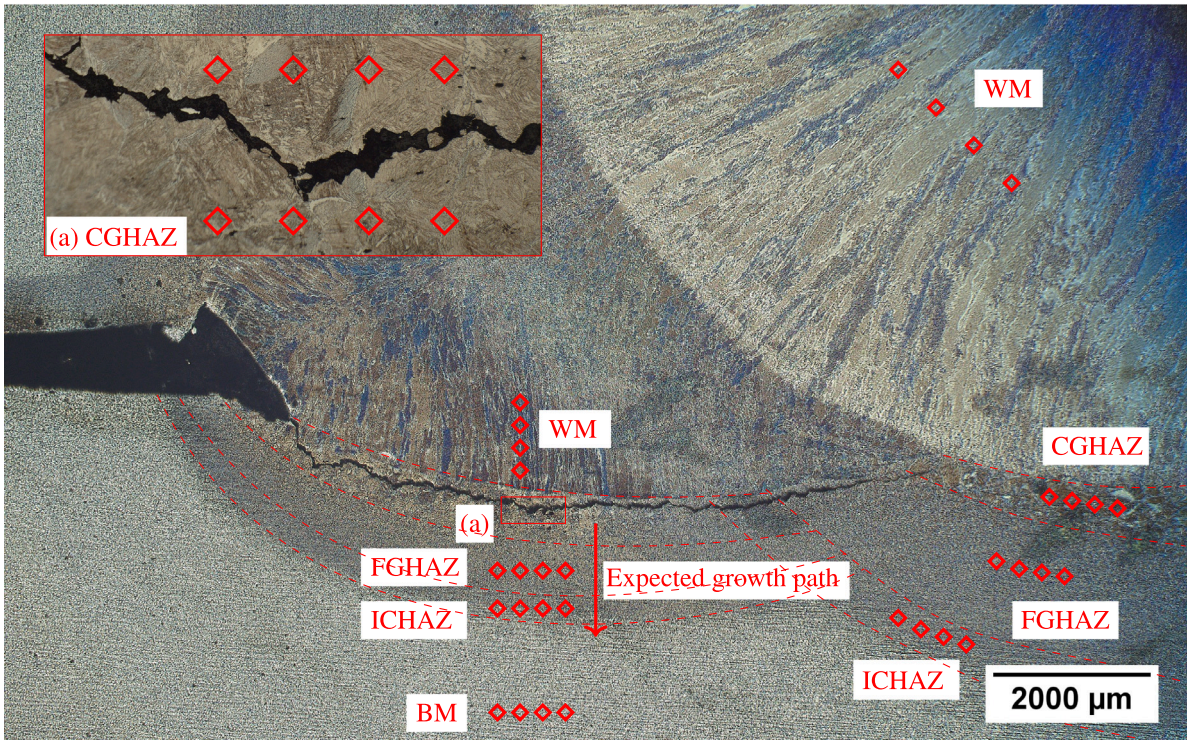


Fig. 14. Vickers Hardness test locations (indicated with ◇) in sample from the bridge containing a cold crack.

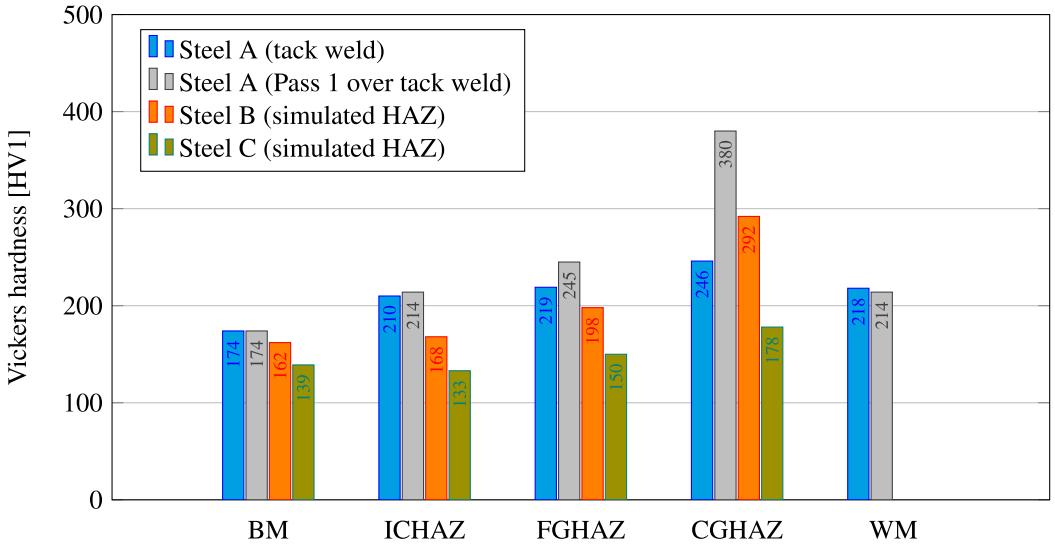


Fig. 15. Hardness results of steel A, B and C. The values are presented inside the bars in HV1.

whether this process could lead to a cold crack-sensitive microstructure. The microstructures in the expected growth path of the initial cold crack were simulated using the Gleeble 3800 apparatus, utilising the temperature–time curves from FEA, and examined by a digital microscope and hardness tests. A method was established for reproducing the subregions of the HAZ on specimens large enough for further (destructive) testing. This method was demonstrated on cold crack sensitive S355 steel and a single pass weld as in the studied T-joint. The main conclusions are:

- The simulation of the tack welding process without preheating in a T-joint resulted in a cooling time $\Delta t_{8/5}$ of 2.0 s. Such a short cooling time is associated with the formation of a cold crack sensitive microstructure, as demonstrated in [25] on steels with comparable compositions to those of Steel A and B of the current study.
- The microstructure of the experimentally simulated ICHAZ showed a combination of unaltered ferrite (with an average grain size of ca. 13 µm and 20 µm for Steel B and Steel C, respectively) and an average size of the refined ferrite and refined pearlite of 2 µm and 4 µm for Steel B and Steel C, respectively. Average sizes of 13 µm and 2 µm were found in Steel A for the unaltered ferrite and refined ferrite/pearlite, respectively, matching with those of Steel B. The refined ferrite/pearlite resulted from base material

pearlite colonies that transformed into austenite upon heating and, upon cooling, transformed into refined ferrite/pearlite.

- The experimentally simulated FGHAZ showed a refined ferrite/pearlite microstructure. In Steel B, an average size of 2 μm was measured for the refined ferrite grains and refined pearlite colonies. In Steel C, an average size of 10 μm and 5 μm was measured for the ferrite grains and pearlite colonies of the FGHAZ, respectively. An average size of 2 μm was found in Steel A for the refined ferrite grains and refined pearlite colonies, matching with those of Steel B. The CGHAZ showed a bainite/martensite microstructure in all steels studied. Both the experimentally simulated FGHAZ and simulated CGHAZ underwent full SSPT.
- The microstructures of the experimentally simulated HAZ subregions of Steel B and Steel C corresponded well with those found in the HAZ subregions of the sample from a bridge.
- The hardness of the CGHAZ of the tack weld (246 HV1), in which the cold crack is present, was significantly lower than the hardness in the CGHAZ of Pass 1 over the tack weld (380 HV1) as a result of tempering by Pass 1 over the tack weld.
- The hardness of the experimentally simulated microstructures of Steel B differed at most 20% with their respective counterpart from the real heat-affective zone of Steel A. Due to a significant lower C_{eq} value, Steel C had a significantly lower hardness compared to Steels A and B for all regions considered. The highest hardness was observed in the CGHAZ for all steels with values of 246, 292 and 178 HV1, for Steels A, B and C, respectively. Steels A and B were found to be sensitive to cold cracking when a tack weld would be applied without preheating whereas Steel C was not.

7. Limitations and future research

The current study focused on the methodology for reproducing the HAZ subregions in specimens large enough for further (destructive) testing. The HAZ was assumed to consist of three discrete subregions, each characterised by a distinct thermal cycle. This three-subregion approach neglects the “smooth” transition between microstructural subgroups. The effect of potential microstructural imperfections near the boundaries between subregions was not investigated. In future research, these specimens will be used in fatigue crack growth tests to study differences in crack growth rates across the various HAZ subregions.

CRediT authorship contribution statement

David Malschaert: Writing – original draft. **Anis Mohabeddine:** Writing – review & editing, Supervision. **Milan Veljkovic:** Writing – review & editing, Supervision. **Davide Leonetti:** Writing – review & editing, Supervision. **Johan Maljaars:** Writing – review & editing, Supervision.

Declaration of competing interest

The authors declare that they have no known competing financial interests or personal relationships that could have appeared to influence the work reported in this paper.

Acknowledgements

This research was carried out under project number T20006c in the framework of the Research Program of the Materials innovation institute (M2i) (www.m2i.nl) supported by Rijkswaterstaat and ProRail. The first author would like to thank Henk Slot for the insightful discussions that benefited this research and Raymond Dekker for the assistance with the experimental set-up.

Data availability

Data will be made available on request.

References

[1] B. Kühn, M. Lukic, A. Nussbaumer, H.-P. Günther, R. Helmerich, S. Herion, M.H. Kolstein, S. Walbridge, B. Androic, O. Dijkstra, et al., Assessment of Existing Steel Structures: Recommendations for Estimation of Remaining Fatigue Life, Joint Research Center, 2008.
[2] M.H. Kolstein, Fatigue Classification of Welded Joints in Orthotropic Steel Bridge Decks, Delft University of Technology, 2007.
[3] C.E. Hartbower, Bridge welding and fracture control, in: Failure Prevention in Ground Transportation Systems, Vol. 621, US Department of Commerce, National Bureau of Standards, 1982, pp. 130–142.
[4] K. Miller, Pay attention to tack and temporary welds, Weld. Innov. 20 (1) (2003).
[5] J.W. Fisher, B.T. Yen, J.H. Daniels, et al., Fatigue damage in the lehigh canal bridge from displacement-induced secondary stresses, Transp. Res. Rec. 607 (1976) 56–62.
[6] S.W. Woods, Rehabilitation of steel deck girder bridges, Transp. Res. Rec. (950) (1984).
[7] S. Jinachandran, J. Xi, G. Rajan, C. Shen, H. Li, B.G. Prusty, Fibre optic acoustic emission sensor system for hydrogen induced cold crack monitoring in welding applications, in: 2016 IEEE Sensors Applications Symposium, SAS, IEEE, 2016, pp. 1–6, http://dx.doi.org/10.1109/SAS.2016.7479896.
[8] W.A. Bruce, J. Proegler, B. Etheridge, S. Rapp, R. Scoles, An alternative approach to time delay prior to inspection for hydrogen cracking, in: International Pipeline Conference, Vol. 51883, American Society of Mechanical Engineers, 2018, V003T05A034, http://dx.doi.org/10.1115/IPC2018-78305.
[9] H.-J. Yi, Y.-J. Lee, J.-Y. Kim, S.-S. Kang, Effect of microstructure and chemical composition on cold crack susceptibility of high-strength weld metal, JMST 25 (2011) 2185–2193, http://dx.doi.org/10.1007/s12206-011-0529-2.
[10] Y. Javadi, N.E. Sweeney, E. Mohseni, C.N. MacLeod, D. Lines, M. Vasilev, Z. Qiu, C. Mineo, S.G. Pierce, A. Gachagan, Investigating the effect of residual stress on hydrogen cracking in multi-pass robotic welding through process compatible non-destructive testing, J. Manuf. 63 (2021) 80–87, http://dx.doi.org/10.1016/j.jmapro.2020.03.043.
[11] F. Matsuda, H. Nakagawa, T. Tsuji, M. Tsukamoto, Effect of hydrogen content on cold crack susceptibility of various steels with the implant test, Trans JWRI 7 (2) (1978) 195–201, http://dx.doi.org/10.18910/10270.
[12] L.H. Hu, J. Huang, Z.G. Li, Y.X. Wu, Effects of preheating temperature on cold cracks, microstructures and properties of high power laser hybrid welded 10Ni3CrMoV steel, Mater. Des. 32 (4) (2011) 1931–1939, http://dx.doi.org/10.1016/j.matdes.2010.12.007.
[13] U. Zerbst, Application of fracture mechanics to welds with crack origin at the weld toe: A review part 1: Consequences of inhomogeneous microstructure for materials testing and failure assessment, Weld. World 63 (6) (2019) 1715–1732, http://dx.doi.org/10.1007/s40194-019-00801-5.
[14] H. Ma, J. Zhao, Y. Fan, Y. Huang, Z. Liu, C. Du, X. Li, Comparative study on corrosion fatigue behaviour of high strength low alloy steel and simulated HAZ microstructures in a simulated marine atmosphere, Int. J. Fatigue 137 (2020) 105666, http://dx.doi.org/10.1016/j.ijfatigue.2020.105666.
[15] K. Easterling, Introduction to the Physical Metallurgy of Welding, Butterworth-Heinemann Ltd, 2013.
[16] J. Xue, W. Guo, Y. Zhang, M. Xia, Q. Jia, J. Chi, J. Shi, Y. Wu, H. Zhang, Local microstructure and mechanical characteristics of HAZ and tensile behavior of laser welded QP980 joints, Mater. Sci. Eng.: A 854 (2022) 143862, http://dx.doi.org/10.1016/j.msea.2022.143862.
[17] D.A. Porter, K.E. Easterling, Phase Transformations in Metals and Alloys (Revised Reprint), CRC Press, 2009.
[18] U. Zerbst, Application of fracture mechanics to welds with crack origin at the weld toe—a review. Part 2: welding residual stresses. Residual and total life assessment, Weld. World 64 (1) (2020) 151–169, http://dx.doi.org/10.1007/s40194-019-00816-y.
[19] J. Martin, Materials for Engineering, Woodhead Publishing, 2006.
[20] P. Kucharczyk, M. Madia, U. Zerbst, B. Schork, P. Gerwien, S. Münstermann, Fracture-mechanics based prediction of the fatigue strength of weldments. Material aspects, Eng. Fract. Mech. 198 (2018) 79–102, http://dx.doi.org/10.1016/j.engfracmech.2017.09.010.
[21] A. Trudel, M. Lévesque, M. Brochu, Microstructural effects on the fatigue crack growth resistance of a stainless steel CA6NM weld, Eng. Fract. Mech. 115 (2014) 60–72, http://dx.doi.org/10.1016/j.engfracmech.2013.11.013.
[22] S. Kim, D. Kang, T.-W. Kim, J. Lee, C. Lee, Fatigue crack growth behavior of the simulated HAZ of 800 MPa grade high-performance steel, Mater. Sci. Eng. A 528 (6) (2011) 2331–2338, http://dx.doi.org/10.1016/j.msea.2010.11.089.
[23] T. Vuherer, F. Smaili, E. Bjelajac, M. Manjgo, G. Lojen, Simulation and mechanical properties of fine-grained heat-affected zone microstructure in 18CrNiMo7-6 steel, Materials 15 (19) (2022) 6782, http://dx.doi.org/10.3390/ma15196782.

[24] F. Smaili, G. Lojen, T. Vuherer, Fatigue crack initiation and propagation of different heat affected zones in the presence of a microdefect, Int. J. Fatigue 128 (2019) 105191, http://dx.doi.org/10.1016/j.ijfatigue.2019.105191.
[25] W. Gao, D. Wang, F. Cheng, X. Di, C. Deng, W. Xu, Microstructural and mechanical performance of underwater wet welded S355 steel, J. Mater. Process. Technol. 238 (2016) 333–340, http://dx.doi.org/10.1016/j.jmatprotec.2016.07.039.
[26] Y. Ito, Y.-i. Komizo, M. Nakanishi, Carbon Equivalent and Hardness for Cracking Tendency of C-Mn Microalloyed Structural Steel, IIW, 1985.
[27] ABAQUS/Standard User's Manual, Version 6.14, Dassault Systèmes Simulia Corp, United States, 2009.
[28] D. Malschaert, M. Veljkovic, J. Maljaars, Numerical simulations of residual stress formation and its effect on fatigue crack propagation in a fillet welded T-joint, Eng. Fract. Mech. (2024) 110236, http://dx.doi.org/10.1016/j.engfracmech.2024.110236.
[29] EN, Recommendations for Welding of Metallic Materials - Part 2: Arc Welding of Ferritic Steels, European Committee for Standardization, 2001.
[30] J. Goldak, A. Chakravarti, M. Bibby, A new finite element model for welding heat sources, MMTB 15 (2) (1984) 299–305, http://dx.doi.org/10.1007/BF02667333.
[31] H. Brandis, Rechnerische Bestimmung Der Umwandlungstemperaturen Von Niedriglegierten Staehlen, CNRS, 1975.
[32] H.K.D.H. Bhadeshia, R.W.K. Honeycombe, Steels: Microstructure and Properties, Butterworth-Heinemann, 2017.
[33] R. Heard, C.R. Siviour, K. Dragnevski, Investigating iron alloy phase changes using high temperature in situ SEM techniques, Materials 15 (11) (2022) 3921, http://dx.doi.org/10.3390/ma15113921.
[34] M. Eroğlu, M. Aksoy, Effect of initial grain size on microstructure and toughness of intercritical heat-affected zone of a low carbon steel, Mater. Sci. Eng. A 286 (2) (2000) 289–297, http://dx.doi.org/10.1016/S0921-5093(00)00801-7.
[35] B.C. Kim, S. Lee, N.J. Kim, D.Y. Lee, Microstructure and local brittle zone phenomena in high-strength low-alloy steel welds, MMTA 22 (1991) 139–149, http://dx.doi.org/10.1007/BF03350956.